analytical chemistry

pubs.acs.org/ac Article

Quadrilateral Nucleic Acid Frame-Accelerating DNAzyme Walker Kinetics for Biosensing Based on Host−Guest Recognition-Enhanced Electrochemiluminescence

Fang Yang, Jia-Shuang Yao, Shu-Chun Bu, Hua-Ying Meng, Ying Zhuo, Xia Zhong,* and Ruo Yuan

Cite This: *Anal. Chem.* 2021, 93, 15493−15500 Read Online

ACCESS | Metrics & More | Article Recommendations | Supporting Information

ABSTRACT: Depending on the reaction between walkers and tracks, DNA walker is able to output signals continuously, which has attracted great attention from the bioanalytical community. Therefore, how to improve its reaction kinetics for efficient signal readout is of great significance. Herein, a quadrilateral DNAzyme walker was fabricated by colocalizing one walker and three DNA tracks in the quadrilateral nucleic acid frame to form a reaction unit (abbreviated as qDNA walker). Impressively, in contrast to the common free DNAzyme walker, the reaction kinetics of the qDNA walker was 2.3 times faster, which could achieve microRNA detection within 30 min. Meanwhile, an electrochemiluminescence (ECL) emitter of anthracene−cucurbituril supramolecular nanocrystals (Ant−CB SNCs) was obtained based on the self-assembly of cucurbituril (CB, host molecule) and anthracene (Ant, guest molecule). Benefiting from the host−guest recognition effect, the prepared Ant−CB SNCs exhibited enhanced ECL efficiency due to the supramolecular interaction between CB and Ant, which could inhibit vibration and rotation of the Ant molecules. We defined this new enhanced ECL phenomenon as "host−guest recognition-enhanced ECL." As a proof of concept, an ECL biosensor for microRNA-21 (miRNA-21) was constructed by combining the high-efficiency DNAzyme walker and the advanced ECL emitter of Ant−CB SNCs, which showed a linear range from 50 aM to 50 pM with a low limit of detection (11 aM), highlighting the great potential in clinical diagnosis.

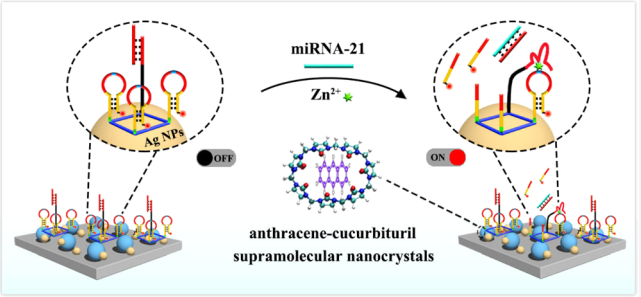

INTRODUCTION

DNA walker is a unique dynamic DNA nanomachine that can move processively along a programmed track. The unique mechanical motion of the DNA walker enables it to perform a variety of tasks to achieve the accumulated signal outputs, providing a valuable platform for molecular transportation and biosensing.[1−5] For example, Le *et al.*[6] assembled both DNA walkers and tracks onto gold nanoparticles (NPs) to form a DNA walker for amyloid *β*-peptide oligomer detection. However, the random assembly of the walkers and tracks is unfavorable for effective collision, reducing the reaction kinetics. By virtue of superior mechanical rigidity and rich modification sites of the frame nucleic acid, our group[7] designed a tetrahedral DNA nanostructure-assisted location-controllable DNA walker with high efficiency, paving the way for sensitive detection of biomarkers. Despite the DNA walker presenting high controllability, the stumbling block is the dependence of nuclease as the driving force, which is of high cost and is vulnerable to environmental interference, restricting its further application in bioanalysis. Herein, a novel quadrilateral DNAzyme walker (qDNA walker) was constructed by colocalizing one walker (Zn^{2+}-dependent DNAzyme) and three DNA tracks in the quadrilateral nucleic acid frame to form a reaction unit. Particularly, the DNAzyme walker supported by the quadrilateral nucleic acid frame not only presented high reaction kinetics but also exhibited better environmental resistance with the DNAzyme as the driving force.

Luminphore, as an important electronic-to-optical transducer in the electrochemiluminescence (ECL) system, has been continuously developed by researchers. As a rising star in luminphores, polycyclic aromatic hydrocarbons (PAHs) have been widely involved in the construction of a sensing platform due to their tunable luminous properties, versatile synthesis, and functional flexibility.[8−10] However, the weak and unstable response of PAHs in aqueous solution slows down their progress in the field of ECL bioanalysis. So far, considerable efforts such as reprecipitation[11] and coassembly[12] have been devoted to improve their stability in aqueous solution to output enhanced ECL signals. It can be inferred that the ordered assembly of luminescent molecules in the confined

Received: August 17, 2021
Accepted: October 26, 2021
Published: November 9, 2021

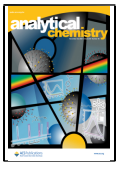

https://doi.org/10.1021/acs.analchem.1c03525
Anal. Chem. 2021, 93, 15493−15500

Scheme 1. Preparation of the qDNA Walker (A), Principle of ECL Biosensor (B), and Preparation of Ant−CB SNCs (C)

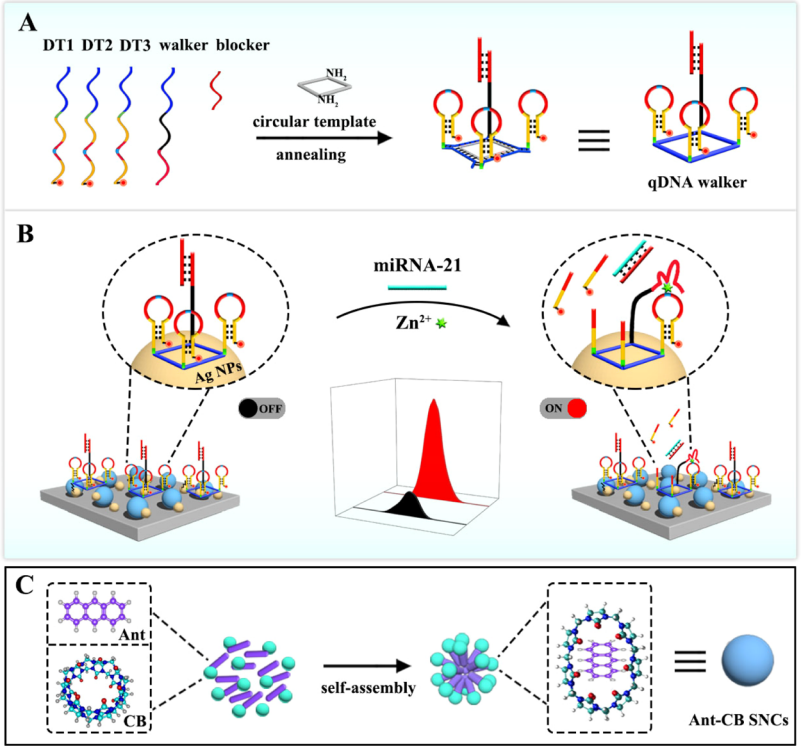

micro/nanospaces could significantly enhance the ECL intensity and efficiency by suppression of nonradiative relaxation and promotion of radiative transition. In this work, an ECL emitter of anthracene−cucurbituril supramolecular nanocrystals (Ant−CB SNCs) was self-assembled by employing the emitter of anthracene (Ant) as the guest molecule and cucurbituril (CB) as the host molecule, demonstrating the advanced ECL performance. It is worth noting that CB in the Ant−CB SNCs could not only suppress the vibration and rotation of the Ant molecules for high-efficiency ECL output due to the host−guest recognition but also act as the coreaction accelerator to accelerate the reduction of $S_2O_8^{2-}$, improving the ECL intensity of Ant−CB SNCs. We define this new enhanced phenomenon as "host−guest recognition-enhanced ECL (HG-ECL)."

Herein, an ECL biosensor for microRNA-21 (miRNA-21) was constructed by combining the high-efficiency DNAzyme walker supported by the quadrilateral nucleic acid frame and the Ant−CB SNCs with advanced ECL performance (Scheme 1). In brief, the Ant−CB SNCs were obtained by the host−guest self-assembly of CB and Ant. Then, the Ag NPs and Ant−CB SNCs were assembled on a glass carbon electrode (GCE) successively to achieve a strong initial signal. Subsequently, the qDNA walker was obtained by self-assembly of the Fc-labeled DNA tracks (DT1, DT2, DT3), walker, blocker, and NH_2-labeled circular template. After that, the qDNA walker was immobilized on the modified electrode through the Ag−N bond to reduce the background signal. In the presence of target miRNA-21, the walker was activated to cleave the DNA tracks with the aid of Zn^{2+}, releasing the Fc labeled DNA fragments to recover the signal. In such a protocol, sensitive detection of miRNA-21 as a model could be realized.

EXPERIMENTAL SECTION

Preparation of Ant−CB SNCs. To obtain the Ant−CB SNCs, 2 mg of Ant powder was dissolved in 1 mL of THF solution and sonicated for 3 min to prepare a homogeneous Ant solution. Meanwhile, 10 mg of CB was dissolved in 5 mL of ultrapure water, and then the Ant solution was quickly transferred into the CB solution. After sonicating for 30 min, the mixture was placed overnight at room temperature. Ultimately, a white precipitate was collected by centrifugation and washing, which was dispersed in 1 mL of ultrapure water for further use.

Preparation of Ag NPs. The Ag NPs were synthesized according to previous report with some modification.[13] In brief, 0.5 mL of 1 M $AgNO_3$ and 2.5 mL of 1 M polyvinyl pyrrolidone (M_w: 40,000) were mixed with 25 mL of PEG-600 in a flask under stirring. The flask was transferred to an oil bath and heated at 100 °C for about 8 h, and then the precipitate was obtained by centrifugation and washing with ethanol and ultrapure water for several times.

Assembly of qDNA Walker. The circular templates were synthesized according to previous report with some modification.[14] Briefly, 5 μL of 100 μM A1, 1 μL of 100 μM padlock, and 14 μL of annealing buffer were consecutively added into a tube, which was heated to 95 °C for 5 min and then cooled down to room temperature slowly within 3 h. After that, the mixture was reacted with T4 DNA ligase in 1× T4 DNA ligase reaction buffer at 16 °C for 12 h to complete the ligation. Subsequently, the ligation product was reacted with EXO I and EXO III to obtain the circular templates, which was finally mixed with DT1 (1 μM), DT2 (1 μM), DT3 (1 μM), walker (1 μM), and blocker (1 μM) to form the qDNA walker.

Fabrication of the Biosensor. First of all, 10 μL of Ant−CB SNCs and Ag NPs were assembled successively on a

https://doi.org/10.1021/acs.analchem.1c03525
Anal. Chem. 2021, 93, 15493−15500

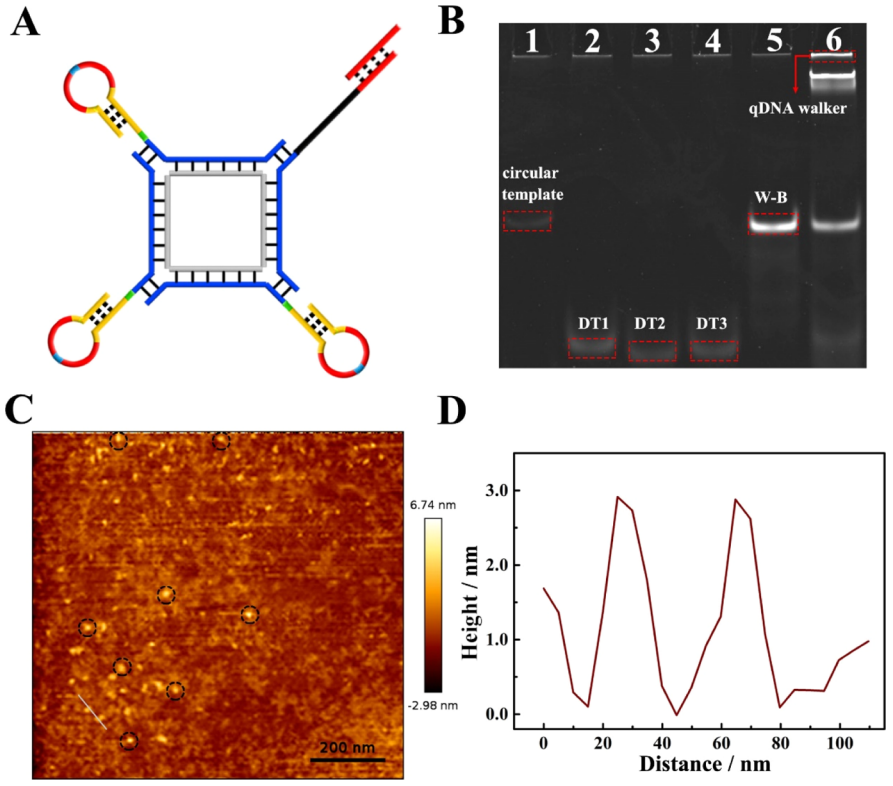

Figure 1. Conformation diagram (A), PAGE characterization (B), AFM image (C), and cross-sectional height profile (D) of the qDNA walker.

cleaned glassy carbon electrode (GCE, Φ = 4 mm) polished with alumina powder to obtain the modified electrode (Ag NPs/Ant−CB SNCs/GCE). Then, 5 μL of qDNA walker was incubated with the modified electrode at 4 °C for 12 h to obtain qDNA walker/Ag NPs/Ant−CB SNCs/GCE through the Ag−N bond. After being rinsed with PBS, 10 μL of hexanethiol (HT, 1mM) was dipped onto the qDNA walker/Ag NPs/Ant−CB SNCs/GCE for 1 h to block nonspecific active sites *via* Ag−S bond. Finally, the above-prepared electrode (HT/qDNA walker/Ag NPs/Ant−CB SNCs/GCE) was stored at 4 °C before determination.

RESULTS AND DISCUSSION

Characterization of qDNA Walker. qDNA walker was characterized by native polyacrylamide gel electrophoresis (PAGE, 8%) and atomic force microscopy (AFM). Figure 1A shows the conformation diagram of the qDNA walker. The PAGE results are shown in Figure 1B; bands 1−5 were circular template, DT1, DT2, DT3, and walker−blocker, respectively. Band 6 was the qDNA walker, which performed a large molecular weight and presented a slow mobility in the electrophoresis bath, indicating that the qDNA walker was assembled successfully. From the typical AFM image of the qDNA walker, it can be seen that the size was about 20 nm. In addition, the qDNA walker diameter was measured to be 3.0 nm by the AFM sectional height analysis (Figure 1D), which was basically consistent with the theoretical value of the DNA double strand.

Kinetic Analysis of DNA Walker. The time-dependent ECL and fluorescence analyses were carried out to study the reaction kinetics of qDNA walker and free DNAzyme walker (fDNA walker, which contained the randomly dispersed walkers and tracks). As shown in Figure 2A, upon the addition of target miRNA-21, the ECL response of the qDNA walker was higher than that of the fDNA walker (Figure 2C). Moreover, from Figure 2B,D, it can be seen that the ECL intensities of the qDNA walker reached a plateau within 30 min, while the fDNA walker required 70 min to reach a plateau. Notably, from the slope obtained by linear fitting of the time-dependent ECL relationship, it was found that the reaction rate of the qDNA walker was 2.3 times faster than that of the fDNA walker, implying the higher reaction efficiency of the qDNA walker.

Subsequently, time-dependent fluorescence analysis of qDNA and fDNA walkers in homogeneous solution was performed to further study their reaction kinetics. Compared with the fDNA walker in homogeneous solution (Figure 2E, blue line), the qDNA walker resulted in an obviously fluorescence recovery. Meanwhile, the completion time for qDNA walker was about 816 s (Figure 2E, red line), which was 5 times faster than that of fDNA walker.

Finally, in order to clarify the high reaction rate and efficiency of the qDNA walker, the reaction process was analyzed using collision theory ($V = 1/cN$)[15,16] in which the V is the local sphere volume, c is the concentration of probes, and N is Avogadro constant. For the qDNA walker, the local concentration of the hairpin is calculated to be 136 μM, which increased by 453 times as compared with the fDNA walker (Figure 2F). The increase in local concentration greatly increases the collision frequency between the walker and DNA tracks in the qDNA walker, accelerating the reaction and improving the reaction efficiency.

DFT Calculations for Ant−CB. To understand the favorable supramolecular interaction between the Ant molecular and CB, the density functional theory (DFT) calculation of quantum chemistry was carried out. As shown in Figure 3A, the optimal molecular configuration of Ant−CB indicated that

https://doi.org/10.1021/acs.analchem.1c03525
Anal. Chem. 2021, 93, 15493−15500

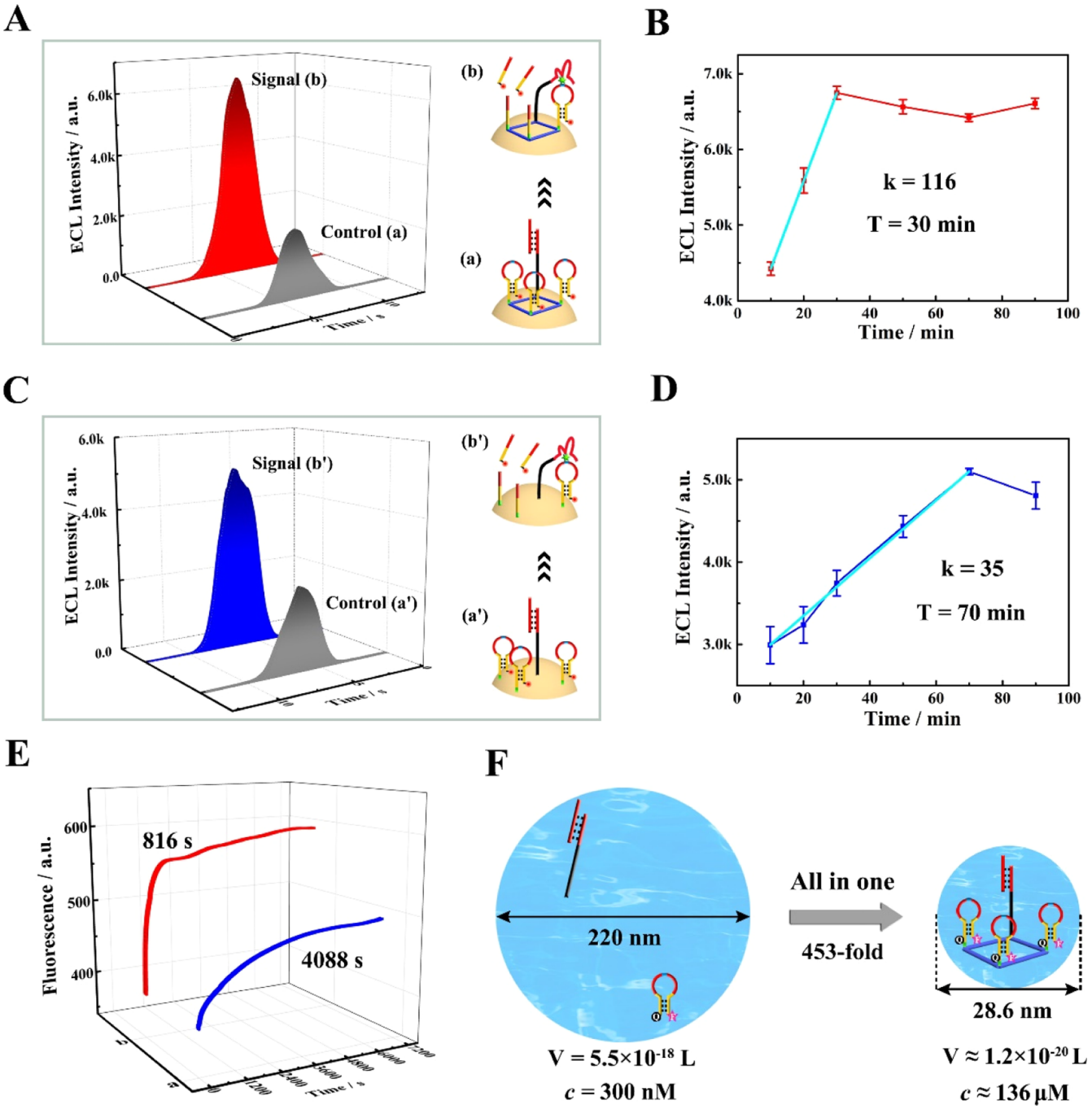

Figure 2. ECL response of the qDNA walker (A) and fDNA walker (C). The insets (a,b) in (A) and (a′,b′) in (C) are the schemes of the qDNA walker and fDNA without and with target, respectively. Time-dependent ECL curve of the qDNA walker (B) and fDNA walker (D). Time-dependent fluorescence analysis of the qDNA walker (red curve) and fDNA walker (blue curve) (E). Comparison of the reaction area and local concentration of DNA tracks in the qDNA walker and fDNA walker (F).

the Ant molecular could form inclusion complex with CB. Furthermore, the independent gradient model (IGM) analysis was also performed to visualize their interaction, and the results are exhibited in Figure 3B,C. There is a spatial region between CB and Ant molecular associated with weak van der Waals interaction. Additionally, the attraction areas in Figure 3B,C intuitively displayed that the binding mode between CB and Ant molecular is multisite and multi-noncovalent binding.

Spectral Characteristics and Fluorescence Imaging Photographs of Ant−CB SNCs. The optical properties of Ant−CB SNCs were studied by ECL and photoluminescence (PL) techniques. As shown in Figure 4A, the PL emission of Ant−CB SNCs was located at 421, 444, and 472 nm, which showed an obvious enhancement compared with the PL emission spectra of Ant nanocrystals (Ant NCs, synthesized by reprecipitation using CTAB as a surfactant). Figure 4B shows the PL decay curve of Ant−CB SNCs, and the average fluorescence lifetime of Ant−CB SNCs was calculated to be 4.0 ns after fitting the PL decay curve with a double-exponential function, which was also higher than that of Ant NCs (3.2 ns, Supporting Information, Figure S3), indicating that the host−guest recognition between CB and Ant could

https://doi.org/10.1021/acs.analchem.1c03525
Anal. Chem. 2021, 93, 15493−15500

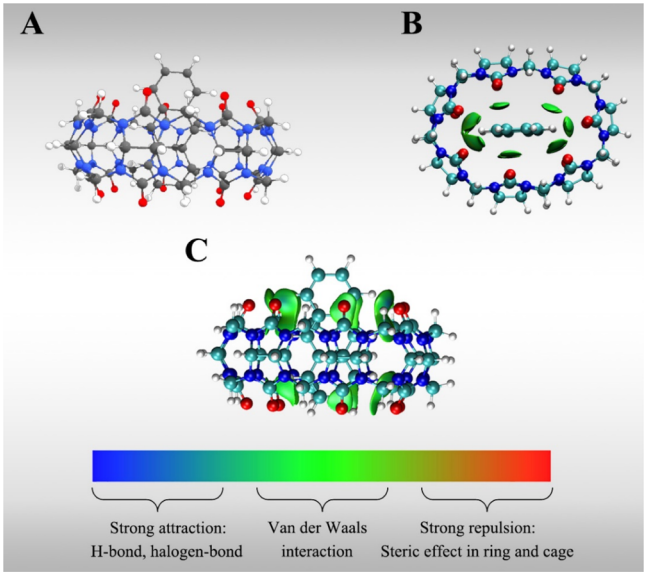

Figure 3. Molecular configuration of (A) Ant−CB. Two different perspectives of the IGM isosurface: top view (B); side view (C).

restrict the molecular vibration and rotation to enhance the emission efficiency.[17] In addition, the morphology of Ant−CB SNCs in the fluorescence microscopic image (Figure 4C) is consistent with SEM imaging (Supporting Information, Figure S1A). Meanwhile, the 3D ECL spectra was applied to trace the evolution of ECL emission (Figure 4D), and an intuitive heat map image of ECL from the Ant−CB SNCs is shown in Figure 4E. In order to know the ECL emission wavelength of the Ant−CB SNCs more accurately, high-resolution 2D ECL spectra were extracted from the 3D ECL spectra (Figure 4F), which showed that the maximum ECL emission of Ant−CB SNCs was located at 597 nm. Compared with the maximum PL emission of Ant−CB SNCs, the ECL emission was red-shifted by 176 nm owing to the different excitation manners of ECL and PL.

Possible Reaction Mechanism of System. In order to investigate the mechanism of CB in the Ant−CB SNCs−$S_2O_8^{2-}$ system, the ECL responses of Ant NCs/GCE and Ant−CB SNCs/GCE were tested at a working potential of −2 to 0 V. As shown in Figure 5A, both Ant NCs/GCE and Ant−CB SNCs/GCE showed a relatively weak ECL intensity in PBS. When they were tested in $S_2O_8^{2-}$ solution, the ECL

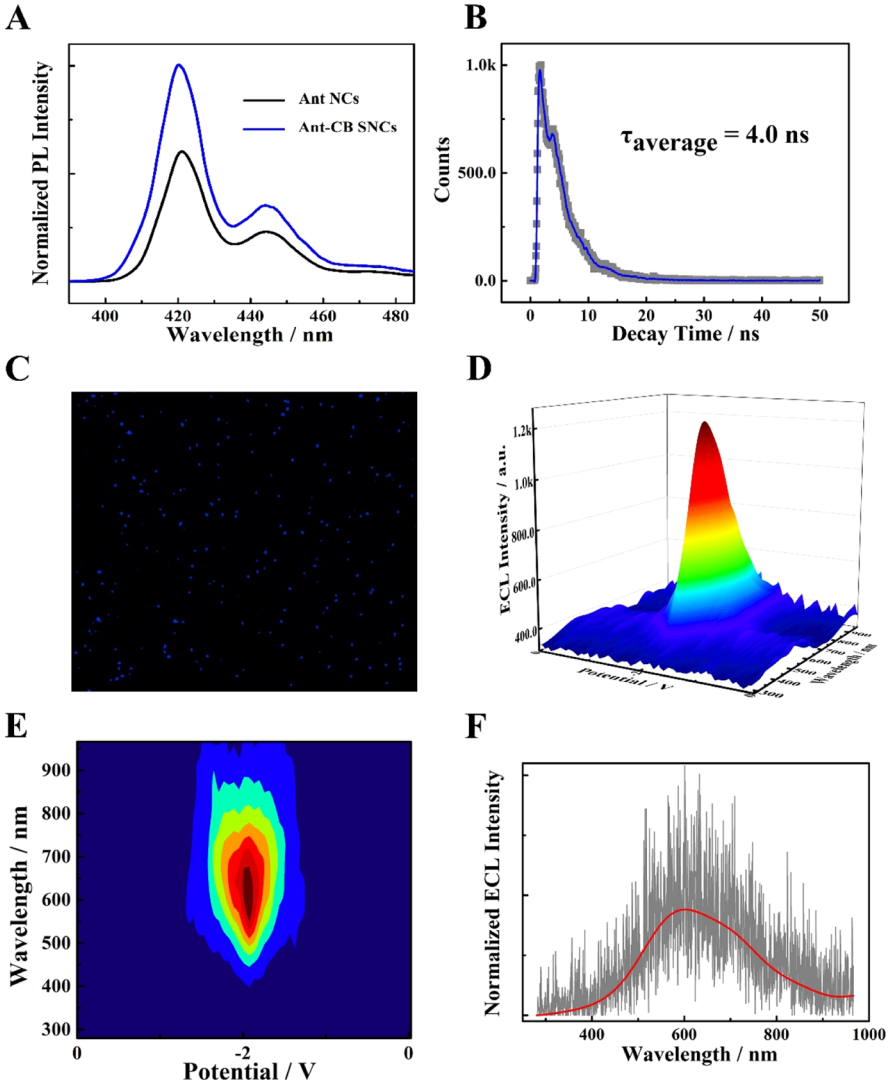

Figure 4. (A) PL spectra of Ant NCs and Ant−CB SNCs (Ex = 365 nm). (B) Time-resolved emission spectra of Ant−CB SNCs. (C) Fluorescence microscopic image of Ant−CB SNCs. (D) 3D surface image, (E) heat map image, and (F) high-resolution 2D ECL spectra of Ant−CB SNCs.

https://doi.org/10.1021/acs.analchem.1c03525
Anal. Chem. 2021, 93, 15493−15500

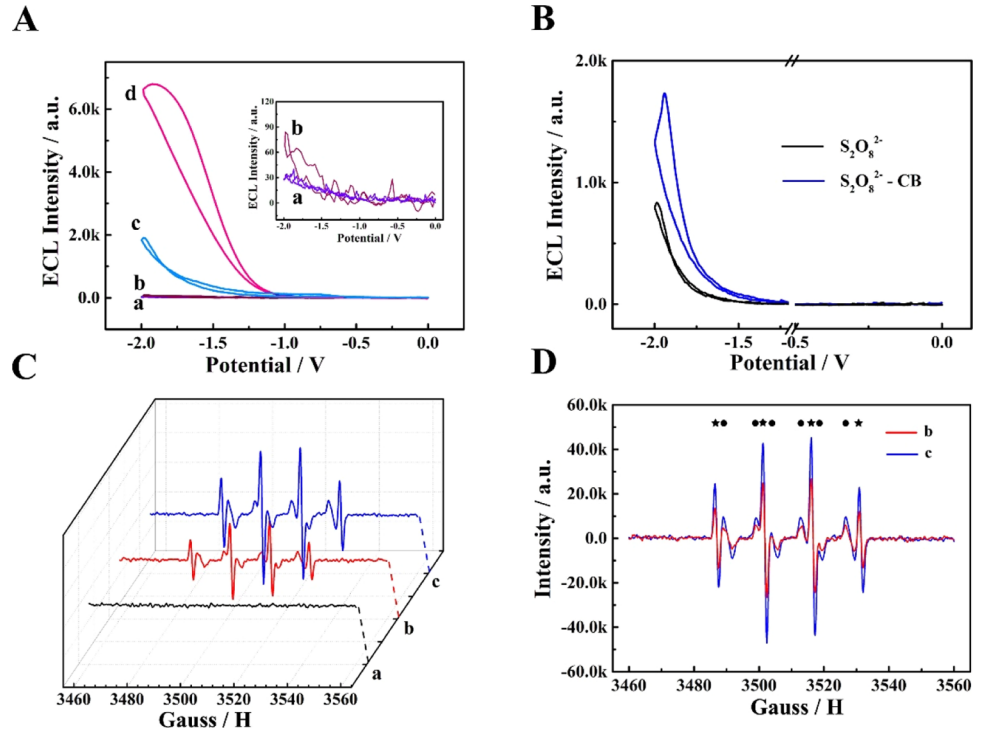

Figure 5. (A) ECL curves of different Ant-modified GCEs: (a) Ant NCs/GCE and (b) Ant−CB SNCs/GCE in 0.1 M PBS, (c) Ant NCs/GCE, and (d) Ant−CB SNCs/GCE in 10 mM $S_2O_8^{2-}$. (B) ECL curve of bare GCE in 10 mM $S_2O_8^{2-}$ (a) and 10 mM $S_2O_8^{2-}$ containing 1 mg/mL CB (b). (C) EPR spectra of 0.1 M PBS containing 100 mM DMPO (a), 10 mM $S_2O_8^{2-}$-100 mM DMPO (b), and CB-10 mM $S_2O_8^{2-}$-100 mM DMPO (c). (D) EPR spectral overlap of curves b and c. "●" stands for the DMPO-SO_4 adduct and "★" stands for the DMPO-OH adduct.

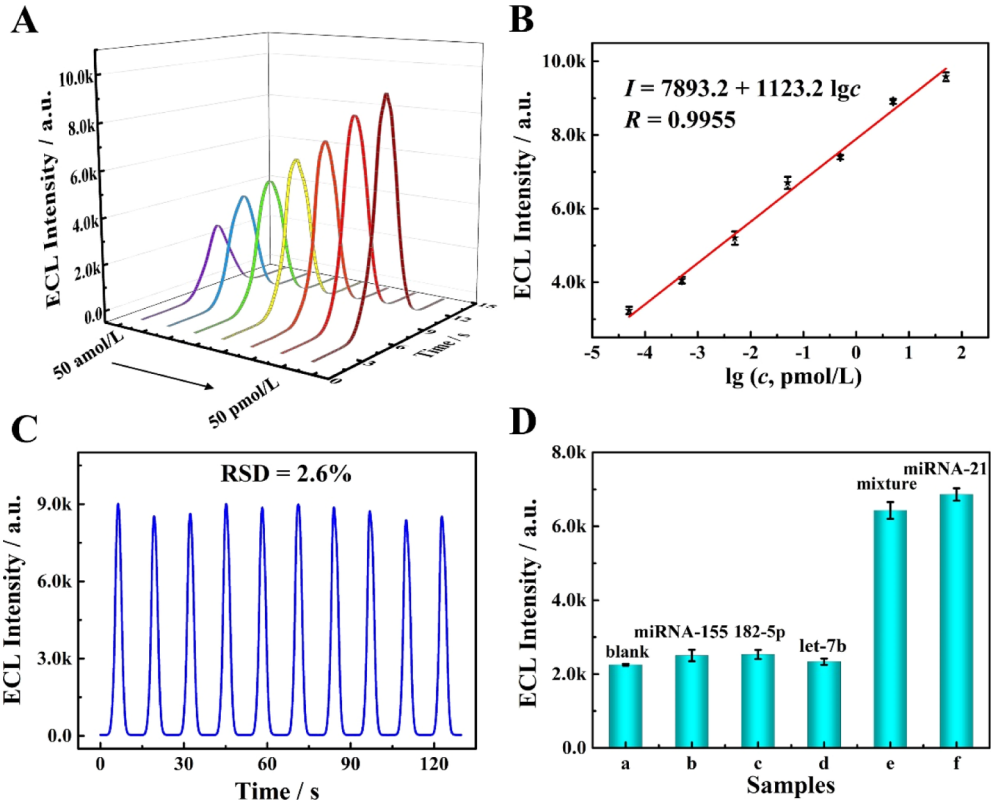

Figure 6. ECL test of the biosensor with miRNA-21 as the model target (A). Calibration curve for the miRNA-21 detection (B). Stability (C) and specificity of the biosensor (D).

responses were significantly enhanced, indicating that $S_2O_8^{2-}$ could act as the coreactant of Ant materials. Furthermore, the ECL intensity of Ant−CB SNCs/GCE (6809 au) was higher than that of Ant NCs/GCE (1907 au) obviously. To verify the

https://doi.org/10.1021/acs.analchem.1c03525
Anal. Chem. 2021, 93, 15493−15500

role of CB, ECL experiments were conducted. As shown in Figure 5B, the ECL intensity of bare GCE in 10 mM $S_2O_8^{2-}$ solution was about 834 au (black curve). After adding CB to the $S_2O_8^{2-}$ solution, the ECL intensity had significantly increased by 2.1 times (1733 au, blue curve). Based on these phenomena, we speculated that CB might be a coreaction accelerator in the Ant SNCs–$S_2O_8^{2-}$ system.

To further investigate the mechanism of CB as a coreaction accelerator in the Ant SNCs–$S_2O_8^{2-}$ system, the radicals in different systems were observed using electron paramagnetic resonance (EPR) analysis with the classic spin-trapping reagent 5,5-dimethyl-1-pyrroline *N*-oxide (DMPO). As shown in Figure 5C, no characteristic signal of active radicals was obtained in the PBS solution (curve a) containing DMPO. However, the EPR signal could be detected in the $S_2O_8^{2-}$ + DMPO solution (curve b, Figure 5C) and $S_2O_8^{2-}$ + DMPO solution containing CB (curve c, Figure 5C). Subsequently, in order to further analyze these data, we overlapped the signals of curve b and curve c. As shown in Figure 5D, four peaks with a 1:2:2:1 quarter pattern (curve b, represented by "black star") could be obviously observed in the $S_2O_8^{2-}$ solution, which was due to the characteristic signal of the DMPO-OH adduct. In addition, the EPR signals of the DMPO-SO_4 adduct were also detected in the $S_2O_8^{2-}$ solution (curve b, Figure 5D, represented by "black circle").[18,19] After the introduction of CB, both DMPO-OH and DMPO-SO_4 adduct signals were enhanced significantly (curve c, Figure 5D), suggesting that CB could promote the reduction of $S_2O_8^{2-}$ to produce more $SO_4^{\bullet-}$.

ECL Analysis of the Sensing Performance for miRNA-21 Detection. The dependence of the biosensor on target concentration was recorded by the ECL technique. As shown in Figure 6A, it was found that the ECL intensity of the biosensor increased with the incensement of the target concentration. The calibration plot in Figure 6B indicated that the ECL intensity was linearly correlated with the logarithmic value of miRNA-21 concentrations in the range from 50 aM to 50 pM. The linear equation was $I = 7893.2 + 1123.2 \lg c$ ($R = 0.9955$). The limit of detection was then calculated to be 11 aM, which was comparable to other developed miRNA-21 biosensors (Table 1). To confirm the stability of the biosensor, continuous scanning (10 cycles) for the biosensor in working buffer was performed in Figure 6C. A relative standard deviation value of 2.6% was calculated from the recorded ECL intensities, demonstrating that the biosensor could meet the needs of the long testing process.

Table 1. Other Methods for miRNA-21 Detection

detection	LOD	linear range	references
SERS	5 fM	12 fM to 18 pM	20
FL	0.72 fM	1 fM to 10 pM	21
EC	37 aM	0.1 fM to 5 pM	22
ECL	0.17 fM	0.5 fM to 10 pM	23
ECL	11 aM	0.05 fM to 50 pM	this work

Furthermore, three potential interfering substances (miRNA-155, 182-5p, and let-7b) were used to investigate the specificity of the biosensor. As shown in Figure 6D, compared with the blank, the ECL intensity of the biosensor incubated with miRNA-155,182-5p, and let-7b had no obvious fluctuation. Compared with the target, the ECL intensity of the biosensor incubated with the mixture containing the three potential interfering substance has no remarkable difference. All of these results indicated that the biosensor has good selectivity.

CONCLUSIONS

In summary, a qDNA walker has been proposed for sensitive detection of miRNA-21 based on Ant–CB SNCs. In the qDNA walker, the walker and tracks were colocalized in a quadrilateral nucleic acid frame. For this point, this strategy not only presents high reaction efficiency due to the colocation of the quadrilateral nucleic acid frame but also exhibited better environmental resistance by using DNAzyme as the driving force. At the same time, the emitter (Ant–CB SNCs) was synthesized by the host–guest recognition between CB and Ant molecules. Specially, CB in the Ant–CB SNCs could suppress the vibration and rotation of the Ant molecules and play as a coreaction accelerator to promote the ECL reaction rate for high-efficiency ECL output, which was defined as "HG-ECL." The work opens up a new way for the DNA walker-based biosensor and holds broad development prospects in the detection of trace biomarkers.

ASSOCIATED CONTENT

Supporting Information

The Supporting Information is available free of charge at https://pubs.acs.org/doi/10.1021/acs.analchem.1c03525.

Materials and reagents, instrumentation, measurement procedure, characterization of the synthesized nanomaterials, characterization of the fabrication process, and spectral characteristics of the Ant NCs (PDF)

AUTHOR INFORMATION

Corresponding Author

Xia Zhong − *Key Laboratory of Luminescence Analysis and Molecular Sensing (Southwest University), Ministry of Education, College of Chemistry and Chemical Engineering, Southwest University, Chongqing 400715, P. R. China*; Phone: +86-23-68253172; Email: zhonglyx@swu.edu.cn; Fax: +86-23-68253172

Authors

Fang Yang − *Key Laboratory of Luminescence Analysis and Molecular Sensing (Southwest University), Ministry of Education, College of Chemistry and Chemical Engineering, Southwest University, Chongqing 400715, P. R. China*

Jia-Shuang Yao − *Key Laboratory of Luminescence Analysis and Molecular Sensing (Southwest University), Ministry of Education, College of Chemistry and Chemical Engineering, Southwest University, Chongqing 400715, P. R. China*

Shu-Chun Bu − *Key Laboratory of Luminescence Analysis and Molecular Sensing (Southwest University), Ministry of Education, College of Chemistry and Chemical Engineering, Southwest University, Chongqing 400715, P. R. China*

Hua-Ying Meng − *Key Laboratory of Luminescence Analysis and Molecular Sensing (Southwest University), Ministry of Education, College of Chemistry and Chemical Engineering, Southwest University, Chongqing 400715, P. R. China*

Ying Zhuo − *Key Laboratory of Luminescence Analysis and Molecular Sensing (Southwest University), Ministry of Education, College of Chemistry and Chemical Engineering, Southwest University, Chongqing 400715, P. R. China*; orcid.org/0000-0002-4491-1186

https://doi.org/10.1021/acs.analchem.1c03525
Anal. Chem. 2021, 93, 15493−15500

Ruo Yuan − *Key Laboratory of Luminescence Analysis and Molecular Sensing (Southwest University), Ministry of Education, College of Chemistry and Chemical Engineering, Southwest University, Chongqing 400715, P. R. China;* orcid.org/0000-0003-3664-6236

Complete contact information is available at: https://pubs.acs.org/10.1021/acs.analchem.1c03525

Notes

The authors declare no competing financial interest.

■ ACKNOWLEDGMENTS

This work was financially supported by the NNSF of China (21904108 and 22022408) and the Fundamental Research Funds for the Central Universities (XDJK2019TJ002).

■ REFERENCES

(1) Chai, H.; Miao, P. *Anal. Chem.* **2019**, *91*, 4953−4957.
(2) Yin, Y.; Chen, G.; Gong, L.; Ge, K.; Pan, W.; Li, N.; Machuki, J. O. a.; Yu, Y.; Geng, D.; Dong, H.; Gao, F. *Anal. Chem.* **2020**, *92*, 9247−9256.
(3) Mason, S. D.; Tang, Y.; Li, Y.; Xie, X.; Li, F. *TrAC, Trends Anal. Chem.* **2018**, *107*, 212−221.
(4) Cheng, X.; Bao, Y.; Liang, S.; Li, B.; Liu, Y.; Wu, H.; Ma, X.; Chu, Y.; Shao, Y.; Meng, Q.; Zhou, G.; Song, Q.; Zou, B. *Anal. Chem.* **2021**, *93*, 9593−9601.
(5) Qi, Y.; Zhai, Y.; Fan, W.; Ren, W.; Li, Z.; Liu, C. *Anal. Chem.* **2021**, *93*, 1620−1626.
(6) Peng, H.; Li, X. F.; Zhang, H.; Le, X. C. *Nat. Commun.* **2017**, *8*, 14378.
(7) Liao, N.; Pan, M.-C.; Wang, L.; Yang, F.; Yuan, R.; Zhuo, Y. *Anal. Chem.* **2021**, *93*, 4051−4058.
(8) Yang, S.-S.; Jiang, M.-H.; Chai, Y.-Q.; Yuan, R.; Zhuo, Y. *ACS Appl. Mater. Interfaces* **2018**, *10*, 38648−38655.
(9) Liu, W.; Chen, A.; Li, S.; Peng, K.; Chai, Y.; Yuan, R. *Anal. Chem.* **2019**, *91*, 1516−1523.
(10) Liao, N.; Zhong, X.; Liang, W.-B.; Yuan, R.; Zhuo, Y. *Acta Chim. Sin.* **2021**, *79*, 1257−1264.
(11) Jiang, M.-H.; Li, S.-K.; Zhong, X.; Liang, W.-B.; Chai, Y.-Q.; Zhuo, Y.; Yuan, R. *Anal. Chem.* **2019**, *91*, 3710−3716.
(12) Liao, N.; Zhang, J. Y.; Huang, Z. Y.; Zhao, Y. X.; Chai, Y. Q.; Yuan, R.; Zhuo, Y. *Chem. J. Chin. Univ.* **2020**, *41*, 1989−1995.
(13) Wei, H.; Reyes-Coronado, A.; Nordlander, P.; Aizpurua, J.; Xu, H. *ACS Nano* **2010**, *4*, 2649−2654.
(14) Tang, J.; Yu, Y.; Shi, H.; He, X.; Lei, Y.; Shangguan, J.; Yang, X.; Qiao, Z.; Wang, K. *Anal. Chem.* **2017**, *89*, 6637−6644.
(15) Zhang, H.; Li, F.; Dever, B.; Wang, C.; Li, X.-F.; Le, X. C. *Angew. Chem., Int. Ed.* **2013**, *52*, 10698−10705.
(16) Ren, K.; Xu, Y.; Liu, Y.; Yang, M.; Ju, H. *ACS Nano* **2018**, *12*, 263−271.
(17) Liu, C.-Y.; Chen, X.-R.; Chen, H.-X.; Niu, Z.; Hirao, H.; Braunstein, P.; Lang, J.-P. *J. Am. Chem. Soc.* **2020**, *142*, 6690−6697.
(18) Cai, X.-L.; Zheng, B.; Zhou, Y.; Younis, M. R.; Wang, F.-B.; Zhang, W.-M.; Zhou, Y.-G.; Xia, X.-H. *Chem. Sci.* **2018**, *9*, 6080−6084.
(19) Dai, P.-P.; Yu, T.; Shi, H.-W.; Xu, J.-J.; Chen, H.-Y. *Anal. Chem.* **2015**, *87*, 12372−12379.
(20) Ma, D.; Huang, C.; Zheng, J.; Tang, J.; Li, J.; Yang, J.; Yang, R. *Biosens. Bioelectron.* **2018**, *101*, 167−173.
(21) Hu, J.; Liu, M.-h.; Zhang, C.-y. *Chem. Sci.* **2018**, *9*, 4258−4267.
(22) Cheng, H.; Li, W.; Duan, S.; Peng, J.; Liu, J.; Ma, W.; Wang, H.; He, X.; Wang, K. *Anal. Chem.* **2019**, *91*, 10672−10678.
(23) Peng, L.; Yuan, Y.; Fu, X.; Fu, A.; Zhang, P.; Chai, Y.; Gan, X.; Yuan, R. *Anal. Chem.* **2019**, *91*, 3239−3245.